Energy 55 (2013) 703–715

Contents lists available at SciVerse ScienceDirect

Energy

journal homepage: www.elsevier.com/locate/energy

The pulse tube engine: A numerical and experimental approach on its design, performance, and operating conditions

Stefan Moldenhauer*, Tilman Stark, Christoph Holtmann, André Thess

Institute of Thermodynamics and Fluid Mechanics, Ilmenau University of Technology, P.O. Box 100565, 98684 Ilmenau, Germany

ARTICLE INFO

Article history:
Received 15 November 2012
Received in revised form
21 March 2013
Accepted 22 March 2013
Available online 4 May 2013

Keywords:
Pulse tube engine
Heat engine
Energy conversion
Waste heat
Thermoacoustics
Modelica

ABSTRACT

The pulse tube engine is a simple heat engine based on the pulse tube process. Due to its simplicity it has a high potential to be applicable in waste heat usage and energy harvesting purposes. In this work, mathematical and experimental design tools are developed to study a pressurized laboratory scale pulse tube engine. The mathematical model is based on the transient numerical solution of the governing differential equations for mass, momentum and energy. The Modelica environment of SimulationX is used to solve the equations numerically and the model is employed to design the experimental test engine with helium as working fluid. The transient behavior of the pulse tube engine's underlying thermodynamic properties is studied numerically and experimentally under different design parameters as well as for different heat input temperatures, filling pressures and operating frequencies. The measured engine characteristics are compared with the calculated predictions. Internal and external power losses are quantified. Design studies for a further development of the pulse tube engine are performed experimentally. The developed numerical tool provides a rational framework for up-scaling the current laboratory model to industrial scale.

© 2013 Elsevier Ltd. All rights reserved.

1. Introduction

The pulse tube engine is a simple prime mover for the conversion of externally supplied thermal power into mechanical power and subsequently into electrical power by using a generator. It represents the thermodynamic counterpart of the pulse tube refrigerator process presented in the 1960's by Gifford and Longsworth [1]. Similar engines were described by Chen at al. [2] and Tailer [3]. The concept of the pulse tube engine was presented by Organ [4] and Hamaguchi et al. [5]. Several experimental investigations to characterize this engine were also published by Hamaguchi et al. [5–7]. A theoretical analysis of pulse tube engine was done by Moldenhauer et al. [8]. It was claimed that a broken thermodynamic symmetry is the underlying working principle of the pulse tube engine. Thermodynamic asymmetry results from the fluidic linkage of an adiabatic space (pulse tube) and an isothermal space (regenerator).

The functional principle of the pulse tube engine is based on the simultaneous compression and motion of the working gas into an area of high temperature of the wall material, followed by a simultaneous expansion and motion of the working gas into an area of low temperature of the wall material.

In spite of the recent modeling attempts [8], the design of pulse tube engines is still largely a matter of intuition and its working mechanisms are not sufficiently well understood. In particular, it would be desirable to possess an experimentally validated simulation tool that would allow reliable extrapolation of the performance of pulse tube engines to higher power ratings. The goal of the present paper is to provide experimental and numerical tools to characterize the mode of operation of the pulse tube engine under different heat input temperatures, filling pressures and operating frequencies, and to find optimal design parameters for future high-performance pulse tube engines.

In Section 2 the functional principle of the pulse tube engine is presented. The developed numerical simulation model is given in Section 3 and the design of the experimental pulse tube engine in Section 4. After the model calibration in Section 5, the experimental test environment is characterized in Section 6. A comparison of the measured and calculated engine performance is presented in Section 7 and the observed influence of design parameters is given in Section 8.

2. Basic design and functional principle of the pulse tube engine

The basic design of the investigated pulse tube engine is shown in Fig. 1. A compression cylinder supplies a pressure swing and gas shifting to the connected system consisting of an adiabatic buffer

* Corresponding author.
E-mail addresses: stefan.moldenhauer@tu-ilmenau.de (S. Moldenhauer), thess@tu-ilmenau.de (A. Thess).

0360-5442/$ – see front matter © 2013 Elsevier Ltd. All rights reserved.
http://dx.doi.org/10.1016/j.energy.2013.03.052

List of symbols

α	heat transfer coeff. [W/(m^2 K)]
Δt	time increment [s]
$\dot{E}$	energy flux [W]
$\dot{E}_{cyc}$	cycle energy flux [W]
$\dot{H}$	enthalpy flux [W]
$\dot{m}$	mass flux [kg/s]
$\dot{Q}$	heat flux [W]
$\dot{Q}_{cg}$	cond. heat flux gas [W]
$\dot{Q}_{cm}$	cond. heat flux mat. [W]
$\dot{Q}_{cyc}$	cycle heat flux [W]
$\dot{Q}_{ext}$	external heat flux [W]
$\dot{Q}_{hx}$	gas-material heat flux [W]
$\dot{Q}_{in}$	supplied thermal power [W]
$\dot{W}$	$pV-$ power [W]
η_n	net efficiency
η_{sh}	shaft efficiency
κ	adiabatic exponent
λ	heat cond. gas [W/(mK)]
μ	dynamical viscosity [Pa s]
ω	cycle frequency [Hz]
ϕ	piston starting position [deg]
$\prod$	pressure ratio
ψ	heat transfer module
ρ	gas density [kg/m^3]
ρ_m	material density [kg/m^3]
τ	temperature ratio
τ_0	minimal temperature ratio
A, B	fitting parameters [Ws, Ws^3]
a, b	fitting functions [W]
A_f	free flow area [m^2]
A_m	material area [m^2]
A_{hx}	heat transfer area [m^2]
c_m	spec. heat capacity [J/(kg K)]
c_p	spec. heat capacity [J/(kg K)]
c_v	spec. heat capacity [J/(kg K)]
d	regenerator diameter [m]
d_h	hydraulic diameter [m]
d_w	wire diameter [m]
e	porosity
F	force [N]
f	operating frequency [Hz]
f_f	flow friction factor
F_f	flow friction force [N]
I	momentum [N m]
L	control volume length [m]
L_r	piston rod length [m]
L_{pt}	pulse tube length [m]
L_{reg}	regenerator length [m]
m	gas mass [kg]
M_{br}	brake momentum [N m]
M_{dr}	drive momentum [N m]
n	number of subvolumes
n_p	polytropie exponent
Nu	Nusselt number
p	pressure [Pa]
p_f	filling pressure [Pa]
P_g	gross power [W]
P_n	net power [W]
$P_{l,ext}$	external power loss [W]
$P_{l,int}$	internal power loss [W]
p_{max}	maximum pressure [Pa]
p_{min}	minimum pressure [Pa]
P_{sh}	shaft power [W]
Pr	Prandtl number
r_c	compression ratio
r_d	distribution ratio
R_s	spec. gas constant [J/(kg K)]
r_{cr}	crank ratio
Re	Reynolds number
s	stroke length [m]
T	gas temperature [°C]
t	time variable [s]
T_c	cold temperature [°C]
T_h	hot temperature [°C]
T_m	material temperature [°C]
T_{chx}	gas temperature chx [°C]
T_{cyl}	gas temperature cylinder [°C]
T_{hhx}	gas temperature hhx [°C]
T_{pt}	gas temp. pulse tube [°C]
T_{reg}	gas temp. regenerator [°C]
u	velocity [m/s]
U_m	internal energy material [J]
V	gas volume [m^3]
V_0	dead volume [m^3]
V_d	displacement volume [m^3]
V_m	material volume [m^3]
V_{hx}	gas vol. heat exchangers [m^3]
V_{max}	max. engine gas volume [m^3]
V_{min}	min. engine gas volume [m^3]
V_{pt}	gas volume pulse tube [m^3]
V_{reg}	gas volume regenerator [m^3]
x	space variable [m]

space (pulse tube) and an isothermalizer (regenerator). Both components are fluidically linked via a gas heater (hhx: hot heat exchanger) at the temperature T_h, providing the heat input. A gas cooler (chx$_1$: cold heat exchanger 1) at the temperature T_c is located between cylinder and pulse tube. To set the depicted material temperature distribution, a heat sink (chx$_2$: cold heat exchanger 2) at the temperature T_c is located at the end of the regenerator.

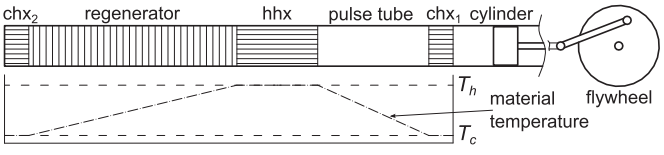

Fig. 1. Basic design of the pulse tube engine: chx$_1$ – cold heat exchanger 1, chx$_2$ – cold heat exchanger 2, hhx – hot heat exchanger.

The conversion of thermal power into mechanical power is enabled by the simultaneous compression and motion of the working gas into an area of high material temperature, followed by a simultaneous expansion and motion of the working gas into an area of low material temperature. Thus, the mean pressure during expansion is higher than during compression resulting in a release of mechanical power. In Ref. [8] was shown that the pulse tube engine is working as a free piston engine. However, enabling the usage of a simple electrical generator, the linear motion of the piston is converted into rotation of a flywheel.

3. Numerical simulation model

A control volume based simulation model is developed. The model is an extension of the ideal pulse tube engine model presented in Ref. [8]. It takes into account dissipative mechanisms such as friction, heat shortcuts due to heat conduction and non-ideal heat transfer.

Fig. 2 shows the schematic representation of the pulse tube engine. Heat can be exchanged between the surroundings and the engine material via the heat flux $\dot{Q}_{ext}$ as well as between the engine material and the working gas via the heat flux $\dot{Q}_{hx}$. In the cylinder the working gas is charged with the compression/expansion power $\dot{W}$. The components are connected at equal pressure through mass fluxes $\dot{m}$ and enthalpy fluxes $\dot{H}$. Due to the high temperature gradients, the pulse tube and the regenerator are each divided into sub control volumes (one-dimensional approximation). The other components consist of one control volume each (zero-dimensional approximation). All entering fluxes are given a positive sign. The following simplifications are made:

1) The flow is one-dimensional.
2) The working fluid is a perfect gas with $p = \rho R_s T$, constant specific heat capacities c_p, c_v and the specific gas constant R_s.
3) The thermodynamic and fluid mechanical properties are uniform within a given control volume.
4) The speed of sound in the working fluid helium has in the temperature range between 20 °C and 600 °C a value higher than 1000 m/s. The typical operating frequency of the pulse tube engine is lower than 100 Hz. For a piston stroke of 50 mm the maximum piston velocity is thus about 10 m/s. The velocity of the fluid has the same order of magnitude. Since the speed of sound is two orders of magnitude higher than the velocity of the fluid, pressure wave reflections at system boundaries are neglected.

3.1. Basic equations and gross power output

The differential equations for pressure p and temperature T of each control volume V are obtained from the ideal model in Ref. [8] with

$$\frac{\mathrm{d}p}{\mathrm{d}t} = \frac{R_s T}{V}\sum \dot{m} - \frac{p}{V}\frac{\mathrm{d}V}{\mathrm{d}t} + \frac{p}{T}\frac{\mathrm{d}T}{\mathrm{d}t}, \tag{1}$$

$$\frac{c_v p V}{R_s T}\frac{\mathrm{d}T}{\mathrm{d}t} = -c_v T\sum \dot{m} + \dot{Q}_{hx} + \dot{Q}_{cg} + \sum \dot{H} + \dot{W}. \tag{2}$$

For the material of the control volume V_m, the conservation equation of the material's internal energy U_m is given by

$$\frac{\mathrm{d}U_m}{\mathrm{d}t} = \sum \dot{Q} = -\dot{Q}_{hx} + \dot{Q}_{cm} + \dot{Q}_{ext}. \tag{3}$$

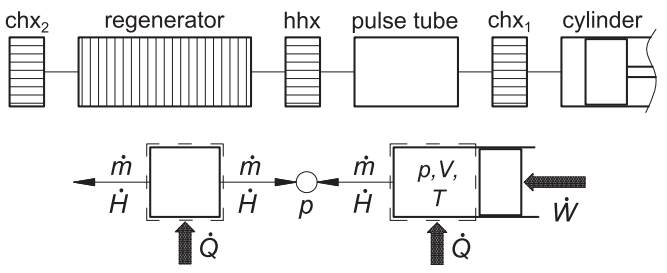

Fig. 2. Schematic representation of the pulse tube engine divided into control volumes with mass and energy fluxes crossing the control volume borders.

With the constant material density ρ_m and the constant specific heat capacity of the material c_m the differential equation for the material temperature T_m can be written in the form

$$\rho_m V_m c_m \frac{\mathrm{d}T_m}{\mathrm{d}t} = -\dot{Q}_{hx} + \dot{Q}_{cm} + \dot{Q}_{ext}. \tag{4}$$

Eqs. (2) and (4) contain additional diffusive terms, $\dot{Q}_{cg}$ and $\dot{Q}_{cm}$, describing the heat conduction within the working gas and the material, respectively.

The heat flux $\dot{Q}_{hx}$ between working gas and material is calculated with the heat transfer area A_{hx} through

$$\dot{Q}_{hx} = \alpha A_{hx}(T_m - T), \tag{5}$$

where the heat transfer coefficient is calculated using $\alpha = Nu\lambda/d_h$, with the Nusselt number Nu, the heat conductivity of the gas λ and the hydraulic diameter d_h. The Nusselt number is obtained from experimental correlations depending on the flow field. For the cylinder, the heat exchangers and the pulse tube, the heat transfer coefficient α is obtained from experimental correlations given in Ref. [9]. Since the porous structure of the regenerator is made of stacked wire mesh screens, experimental correlations for α from Ref. [10] are used. The heat transfer area A_{hx} in the regenerator with the length L_{reg} and the diameter d_{reg} is given by

$$A_{hx} = e(1-e)\frac{\pi d_{reg}^2 L_{reg}}{d_w}, \tag{6}$$

where e is the regenerator porosity and d_w the wire diameter of the mesh. The heat transfer coefficient is calculated according to [10] from

$$\alpha = \psi \frac{c_p \mu}{d_h}\frac{Re}{Pr^{2/3}}, \tag{7}$$

with the dynamical viscosity μ, the Reynolds number Re and the Prandtl number Pr. The heat transfer module ψ is calculated according to

$$\psi = \left(2.128 - 8.591e + 9.6878e^2\right)\mathrm{Re}^{-0.113-0.475e}. \tag{8}$$

The cylinder volume varies in time and is given by

$$V(t) = V_0 + \frac{V_d}{2}\left(1 + r_{cr} - \cos(\omega t - \varphi) - \sqrt{r_{cr}^2 - \sin^2(\omega t - \varphi)}\right), \tag{9}$$

where the crank ratio $r_{cr} = 2L_r/s$ is the ratio between piston rod length L_r and crank radius $s/2$, which is half of the stroke s. The cycle frequency is defined by $\omega = 2\pi f$ and the starting position of the piston is given by φ, where $\varphi = 0$ at the piston's top dead center (TDC). The piston's bottom dead center is denoted with BDC. The dead volume and the displacement volume are represented by V_0 and V_d.

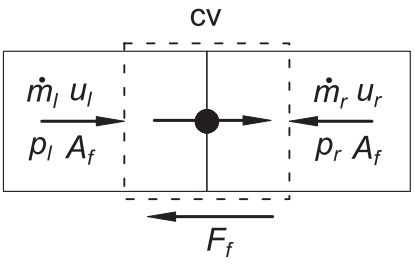

Fig. 3. Acting pressure forces, momentum forces and the friction force on the control volume gas mass. l = left side, r = right side.

Using Eqs. (1)–(4), the gross power output P_g of the pulse tube engine can be calculated.

3.2. Net and shaft power output

The engine's gross power output is reduced by internal power losses $P_{l,\mathrm{int}}$, mainly due to friction between gas and filling material as well as heat transfer. In order to calculate the net power output P_n of the engine, the equation of motion is added to the model.

The momentum balance is given by

$$\frac{\mathrm{d}I}{\mathrm{d}t} = \sum F, \tag{10}$$

where $I = mu$ represents the momentum of the gas element m having the velocity u. Forces on the gas element are represented by F. With the expression $\dot{m} = \rho A_f u$, which relates the mass flux $\dot{m}$ with the velocity, the free flow area A_f and the gas density $\rho = m/V$ follows

$$u = \frac{\dot{m}}{\rho A_f} = \frac{V\dot{m}}{mA_f} = L\frac{\dot{m}}{m}, \tag{11}$$

where L represents length of the control volume (cv). Using Eq. (11), the momentum results in $I = mu = \dot{m}L$ and thus Eq. (10) in

$$\frac{\mathrm{d}I}{\mathrm{d}t} = L\frac{\mathrm{d}\dot{m}}{\mathrm{d}t} = \sum F. \tag{12}$$

According to Fig. 3 momentum forces are calculated with $\dot{m}u = L\dot{m}^2/m$ and pressure forces with pA_f. The flow friction force is represented by F_f. Hence, together with the thermal state equation of a perfect gas, Eq. (12) becomes

$$\frac{\mathrm{d}\dot{m}}{\mathrm{d}t} = \dot{m}_l^2\frac{R_s T_l}{p_l V} - \dot{m}_r^2\frac{R_s T_r}{p_r V} + \frac{A_f}{L}(p_l - p_r) - \frac{F_f}{L}. \tag{13}$$

According to [10] the flow friction force can be modeled using

$$F_f = f_f\frac{2\dot{m}|\dot{m}|L}{\rho A_f d_h}, \tag{14}$$

where f_f represents a flow friction factor.

The temporal change of the mass flux $\dot{m}$ becomes finally

$$\frac{\mathrm{d}\dot{m}}{\mathrm{d}t} = \frac{R_s}{V}\left(\frac{\dot{m}_l^2 T_l}{p_l} - \frac{\dot{m}_r^2 T_r}{p_r}\right) + \frac{A_f}{L}(p_l - p_r) - f_f\frac{2\dot{m}|\dot{m}|}{\rho A_f d_h}. \tag{15}$$

The use of the absolute value for the mass flux ensures that the direction of the flow friction force is opposite to the direction of motion.

The gas flow in the cylinder, the heat exchangers and the pulse tube has low Reynolds numbers ($Re < 1000$), so that the friction factor relation $f_f = 16/Re$ for laminar flow is applicable. In the regenerator even lower Reynolds numbers ($Re < 100$) are present. According to [11,12] the flow field in porous media can be turbulent at low Reynolds numbers, too. To calculate the friction force in the regenerator an experimental friction factor correlation from Ref. [10] is used. The friction factor relation $f_f = 16/Re$ and the friction factor correlation from Ref. [10] are valid for fully developed stationary flows, but also used for the present transient analysis. The induced modeling error resulting from this is judged to have minor importance compared to the error induced by the one-dimensional modeling.

To get the shaft power output P_{sh}, the net power has to be reduced by an amount equaling the power losses due to friction in the cylinder, the bearings and the crank mechanism. The friction force in the cylinder is proportional to the constant gravity force of the piston and piston rod. For the crank mechanism the friction force in the linear and rotating bearings is a superposition of the constant gravity force of the rod and the shear force caused by the crank mechanism. The shear force is proportional to the square of the operating frequency f^2. Thus, the total friction power loss $P_{l,\mathrm{ext}}$ in the cylinder and the crank shaft can be modeled according to

$$P_{l,\mathrm{ext}}(f) = Af + Bf^3, \tag{16}$$

where the influence of the filling pressure variation is neglected and A and B are constant fitting parameters. The shaft power output can then be calculated from $P_{\mathrm{sh}} = P_n + P_{l,\mathrm{ext}}$, with the convention that any power delivered by the engine has a negative sign.

The model has two free parameters which need to be quantified. These are the dead volume V_0 and the starting position of the piston φ in degree of crank angle relative to TDC. Both parameters will be determined experimentally.

3.3. Computation parameters

The system of differential equations is solved numerically using the object-oriented programming language Modelica within the software SimulationX. With the correct initial conditions, the dynamical state variables of the pulse tube engine such as the gas temperatures $\{T_{\mathrm{cyl}}(t),\ T_{\mathrm{chx}_1}(t),\ T_{\mathrm{chx}_2}(t),\ T_{\mathrm{hhx}}(t),\ T_{\mathrm{pt}}(x,t),\ T_{\mathrm{reg}}(x,t)\}$ are obtained. The cycle energy fluxes $\dot{E}_{\mathrm{cyc}}$ are calculated by integrating the energy fluxes $\dot{E}$ over one engine cycle and multiplying the result with the operating frequency f. As an example, the cycle heat flux of a component and the net cycle power are given by $\dot{Q}_{\mathrm{cyc}} = f\oint \dot{Q}\mathrm{d}t$ and $P_n = f\oint \dot{W}\mathrm{d}t$. For all calculations a sufficient number of engine cycles is calculated until the changes from cycle to cycle are negligible. The values of $\dot{Q}_{\mathrm{cyc}}$ and P_n are averaged over the last ten cycles.

The calculations are performed with minimum and maximum permissible time increments of $\Delta t_{\min} = 10^{-8}$ s and $\Delta t_{\max} = 10^{-5}$ s, and a number of subvolumes for pulse tube and regenerator of $n = L_{\mathrm{pt/reg}}/2$, where $L_{\mathrm{pt/reg}}$ are the lengths of the components measured in millimeters.

4. Design of the experimental pulse tube engine

The simulation model is used to design an experimental test engine. The aim of the experimental set-up is to validate the simulation model. Furthermore, the experimental test engine is also used to study the pulse tube engine's performance for different designs and operation conditions.

4.1. General engine design

The general design of the test engine is shown in Fig. 4. It has a cylinder with a bore of 24 mm and a variable stroke between 20 mm and 100 mm. The cylinder is a low friction AIRPEL (Airpot cooperation) pneumatic cylinder with a glass liner and a piston made of aluminum and graphite. The front side of the cylinder is connected to a water cooled copper heat exchanger (chx_1). The pulse tube, the hot heat exchanger (hhx) and the regenerator are placed in a stainless steel tube with an inner diameter of 20 mm and a total length of 230 mm (including flanges). An electrical resistance heater is place inside the hot heat exchanger. At the cold side of the regenerator a second water cooled heat exchanger (chx_2) is located.

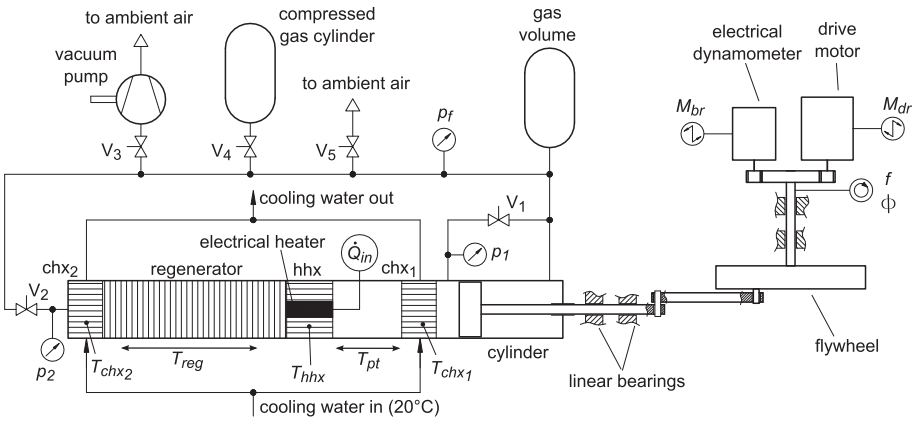

Fig. 4. Structure of the experimental set-up.

4.2. Model based design of the components

Two parameters characterizing the design of the pulse tube engine – the compression ratio r_c and the distribution ratio r_d – are introduced. The compression ratio is defined as

$$r_c := \frac{V_{\mathrm{pt}} + V_{\mathrm{reg}} + V_{\mathrm{hx}} + V_d}{V_{\mathrm{pt}} + V_{\mathrm{reg}} + V_{\mathrm{hx}}} - 1 = \frac{V_d}{V_{\mathrm{pt}} + V_{\mathrm{reg}} + V_{\mathrm{hx}}} \tag{17}$$

and the distribution ratio as

$$r_d := \frac{V_{\mathrm{reg}}}{V_{\mathrm{pt}}}, \tag{18}$$

where V_{reg} and V_{pt} are the regenerator and the pulse tube volume, V_d is the displacement volume of the cylinder and V_{hx} is the sum of the heat exchanger volumes. Engine power output and efficiency have strong dependencies on the optimal choice of r_c and r_d. The present engine was designed to vary these values in a later optimization process. The distribution ratio was first set to $r_d = 1.51$. Using a stroke of 40 mm the compression ratio is $r_c = 0.38$.

The regenerator is located at one side of the stainless steel tube. Therefore it is filled with stacked stainless steel wire mesh screens having a mesh number of 50 and a wire diameter of 200 μm. The length of the regenerator is 122 mm. Its porosity is 0.67 and the total regenerator mass is about 200 g. In the middle of the tube the hot heat exchanger with a length of 40 mm is located. The rest of the tube (68 mm) is used as pulse tube. A spacer with 10 mm in diameter and 40 mm in length is placed on the pulse tube axis in order to reduce its gas volume. Both water cooled cold heat exchangers are made from copper. The cold heat exchanger chx_2 at the regenerator's cold side has a 2 mm in diameter bore and a closed end. The cold heat exchanger chx_1 with a length of 11 mm at the pulse tube's cold side has a spark-eroded structure to achieve a certain heat transfer structure.

Heat input is provided by an electrical resistance heater and delivered to the working gas via the hot heat exchanger. Its heat transfer area has no theoretical limitation and was designed to be as large as possible. In contrast, the cold heat exchanger chx_1 needs a certain heat transfer area to allow optimal engine operation. To get the optimal heat transfer area, which maximizes the engine's power output, the simulation model was used. The calculated optimal heat transfer area is 56 cm^2.

The resulting values of the gas and material volume, V and V_m, as well as of the free flow area A_f, the material area A_m, the heat transfer area A_{hx} and the hydraulic diameter d_h are listed in Table 1. The maximum and minimum gas volume of the engine are given by

$$V_{\max} = V_d + V_0 + V_{\mathrm{pt}} + V_{\mathrm{reg}} + V_{\mathrm{hx}} \tag{19}$$

and

$$V_{\min} = V_0 + V_{\mathrm{pt}} + V_{\mathrm{reg}} + V_{\mathrm{hx}}, \tag{20}$$

where V_0 represents the sum of the dead volumes of the cylinder as well as of the connected tubes and valves. The dead volume V_0 is at low temperature and can entirely be regarded as cylinder dead volume. It is split into a known (measurable) dead volume V_0^a and an unknown dead volume V_0^b. The measured known dead volume is $V_0^a = 7.5\,\mathrm{cm}^3$ and the free parameter V_0 is replaced by the free parameter V_0^b. Its value is calculated from pressure measurements after building up the engine. According to [8] it partly represents virtual dead volume due to leakage between piston and cylinder liner.

4.3. Experimental set-up and operating conditions

The structure of the experimental set-up is shown in Fig. 4. The rear side of the cylinder is connected to an external gas volume simulating a pressurized environment. The engine is filled with pressurized helium up to a filling pressure of $p_f = 12$ bar. The piston front and rear side have a connecting tube, which can be opened and closed using valve V_1. This bypass tube allows to run the cylinder without any pressure swing in the system and almost no gas passing chx_1. The cold heat exchanger chx_2 can be opened and closed to the gas volume using valve V_2. This allows to fill the engine with pressurized gas without having V_1 opened. The whole system is connected to a vacuum pump via valve V_3 and a compressed gas cylinder via valve V_4. The system can be emptied to the ambient by opening valve V_5. The filling pressure is measured using a mechanical pressure gauge with a precision of 0.25 bar.

The piston rod is guided by linear bearings. The linear movement is transformed into rotation via a crank shaft mechanism. The

Table 1
Geometrical parameters of the engine components.

Parameter	chx_2	Regenerator	hhx	Pulse tube	chx_1	Cylinder
V [cm^3]	1.8	25.6	2.8	16.9	0.8	21…39[a]
V_m [cm^3]	–	20.8	2.4	4.5	1.8	–
A_f [cm^2]	0.1	2.1	0.7	2.4	0.8	4.5
A_m [cm^2]	–	1.7	2.4	0.7	1.6	–
A_{hx} [cm^2]	18	1700	187	43	56	44…74[a]
d_h [mm]	4	0.4	0.6	10	0.6	24

[a] Oscillating.

connected flywheel serves as rotational energy storage for the compression stroke. Two electrical motors are connected to the flywheel. One is used as electrical dynamometer to apply a brake momentum on the engine. The resulting electrical current is measured and used to calculate the brake momentum M_{br}. The second electrical motor serves as a drive to motor the engine. The electrical current of the drive motor is also measured to calculate the drive momentum M_{dr}.

The electrical heater, placed inside the hot heat exchanger has a maximum permissible temperature of 700 °C and a maximum thermal power of 160 W. The heater temperature is measured and controlled using a two-level controller. It can be fixed between 40 °C and 650 °C. The cold heat exchangers are water cooled with a cooling water inlet temperature of 20 °C.

4.4. Measurement techniques

In order to characterize the pulse tube engine in operation, the signals of various sensors and measuring devices are monitored. The main measured quantities are temperatures T, the supplied thermal power $\dot{Q}_{in}$, brake and drive torques M_{br} and M_{dr}, the working gas pressure p, the operating frequency f and the crank angle of the flywheel φ. The measured temperatures are in particular the temperatures of the heat exchangers T_{chx_1}, T_{chx_2} and T_{hhx}, as well as the temperature profiles of the regenerator T_{reg} and the pulse tube T_{pt}. A scheme of the measurement is shown in Fig. 5.

The thermal power input $\dot{Q}_{in}$ is calculated from the measured voltage and current of the heater power supply. Heat losses are quantified experimentally in Section 6.1. The torques of the two electrical motors M_{br} and M_{dr} are calculated from its electrical currents, which are correlated to measured voltages of shunts. The current of the brake motor is smaller than of the drive motor. To increase the accuracy three switchable shunts are used. The measured voltages are amplified and processed by a micro controller. To ensure the highest possible precision, the amplification circuits were checked for their linearity before the measurements. The conversion factors between the measured voltages and the quantities to be identified were determined by calibrations. The values are stored in the micro controller Flash-EEPROM.

The working gas pressure is recorded using piezoresistive pressure sensors p_1 and p_2 between chx_1 and the cylinder as well as at chx_2. The sampling rate is 4 kHz. The voltage signals are logged by a data acquisition system and monitored with a personal computer (PC). Operating frequency f and crank angle φ are measured by two light barriers at the interrupt input of the micro controller. The first light barrier is interrupted 20 times per revolution of the motor shaft, thus permitting a frequency measurement with an accuracy of 0.05 Hz. The determination of the crank angle becomes possible with the second light barrier which is interrupted only once per revolution and thereby setting the zero position of the crank angle. Each other interruption of the light beam of the first barrier increases the value of the crank angle by 18°. The crank angle is converted into a voltage between zero and 5 V via pulse width modulation and then forwarded to the data acquisition system and the personal computer. With this data the pV-diagram of the engine can be monitored.

The temperatures are measured with K-type thermocouples. The thermoelectric voltages are converted into temperatures by an AGILENT 34970A transducer with built-in reference junction. The data are transmitted via the RS232 interface every 2 s to the personal computer. The thermoelectric voltage of the thermocouple placed at the hot heat exchanger is also amplified externally and read with the micro controller. The signal is used to control the heater temperature with a two-level controller.

The errors of the measured quantities are listed in Table 2. For the non-derived quantities f, p_f, T_{chx}, T_{hhx}, T_{pt}, T_{reg}, M_{br}, M_{dr} and $\dot{Q}_{in}$ the listed relative or absolute errors are systematic errors of the measurement set-up. For the derived quantities P_{sh}, P_n, η_{sh} and η_n the systematic errors are obtained through the law of error propagation. Using the electrical dynamometer the minimum absolute error of the shaft power is quantified experimentally to 0.1 W. Measuring the shaft power or the net power with the electrical drive motor the minimum absolute error is quantified experimentally to 0.4 W.

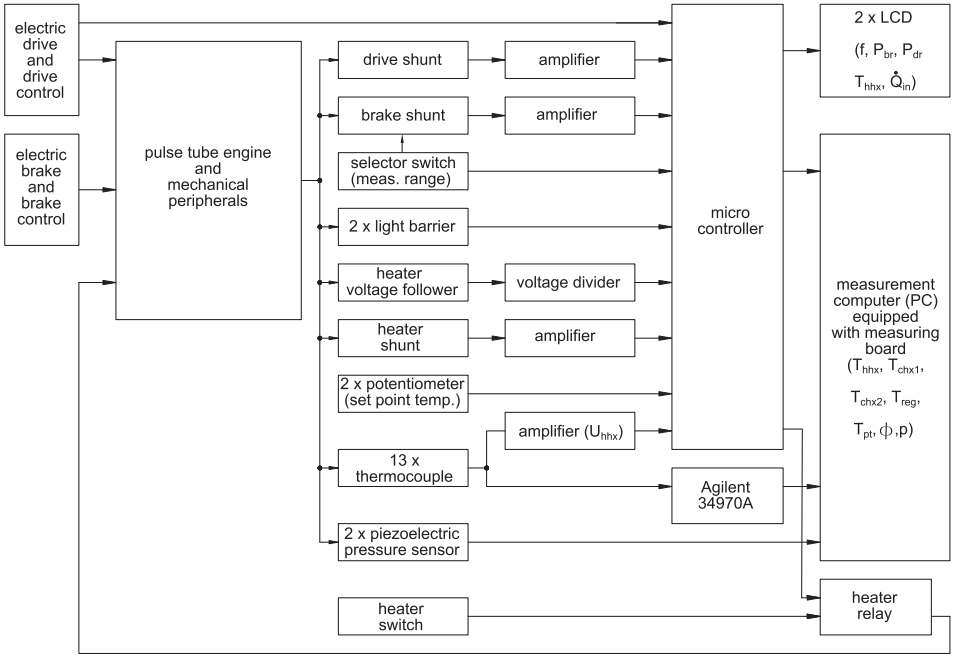

Fig. 5. Structure of the data acquisition system.

Table 2
Systematic errors of the measured quantities.

Measured quantity	Max. relative error	Min./fix absolute error
f	1%	Min. 0.05 Hz
p_f	–	Fix 0.25 bar
T_{chx}	–	Fix 1 K
T_{hhx}	–	Fix 15 K
T_{pt}, T_{reg}	–	Fix 30 K
M_{br}, M_{dr}	10%	–
$\dot{Q}_{in}$	4%	–
P_{sh}	11%	Min. 0.1 W[a]
P_{sh}, P_n	11%	Min. 0.4 W[b]
η_{sh}, η_n	15%	–

[a] Using the electrical dynamometer.
[b] Using the electrical drive motor.

5. Model calibration

The free parameters which need to be quantified are the unknown dead volume V_0^b (see Section 4.2) and the starting position of the piston φ (see Section 3). Both values were obtained from the measured time-dependent pressure at ambient temperature. The parameters V_0^b and φ were varied to minimize the error of the calculated minimum pressure and the calculated pressure amplitude for filling pressures between 6 bar and 10 bar and a mean engine frequency of 8 Hz. The results are $\varphi = 76$ deg and $V_0^b = 13.5\,\text{cm}^3$. Thus, the total additional dead volume of the engine is $V_0 = 21\,\text{cm}^3$. A comparison of the calculated and measured time-dependent pressure is shown in Fig. 6. The relative differences between the measured and calculated minimum pressure and pressure amplitude are smaller than 2.5% and 3.2%, respectively.

6. Characterization of the experimental test environment

To characterize the experimental set-up and to quantify the measured power values, the thermal power loss of the electrical heater and the power dissipation in the cylinder and the crank mechanism are investigated.

6.1. Measured versus calculated thermal power input

The engine was run at $T_h = 600\,^\circ\text{C}$, $T_c = 25\,^\circ\text{C}$ and filling pressures between 6 bar and 10 bar. The electrical dynamometer was used to apply a brake momentum on the engine. A comparison of the measured and calculated thermal power input is given in Fig. 7. The power input was measured from the electrical power consumption of the heater placed inside the hot heat exchanger. The measured thermal power input is between 40% (10 bar, 8 Hz) and 95% (6 bar, 4 Hz) higher than the calculated thermal power input. The reason is that not all the heat power is transferred to the working gas. A part of it is lost to the ambient air. However, calculated and measured heat power input increase with the operating frequency at an average slope of about 7.2 W/Hz.

The calculation predicts a monotonic increase of the thermal power input with the filling pressure. In the experiment the thermal power input increases only between 6 bar and 8 bar of filling pressure. For filling pressures higher than 8 bar, the measured thermal power input decreases. A reason for this behavior could be a smaller temperature difference between the working gas and the heat exchanger material and thus a lower entropy production during the heat transfer process.

6.2. Friction power loss in the cylinder and the crank mechanism

The friction power loss in the cylinder and the crank mechanism was measured for filling pressures between 6 bar and 10 bar and frequencies between 4 Hz and 12 Hz. To do so, the engine was motored using the drive motor while valve V_1 was open. Thus, no compression occurred in the cylinder. The result is shown in Fig. 8. The observed influence of the filling pressure on the friction power loss is small. According to Section 3.2 the friction power was averaged over all filling pressures at each frequency and fitted using Eq. (16). The resulting fitting parameters are $A = 0.301 \pm 0.022$ Ws and $B = 0.005 \pm 0.001$ Ws^3.

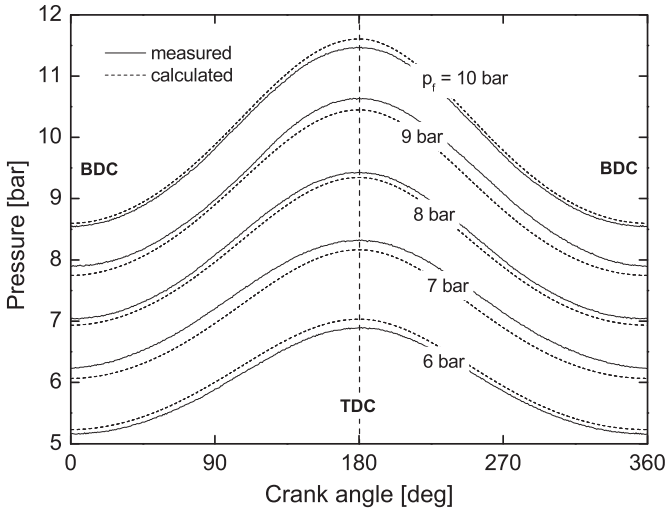

Fig. 6. Calculated and measured time-dependent pressure as functions of the crank angle for different filling pressures.

6.3. Sign convention

For all considerations in Sections 7 and 8 heat power inputs, mechanical power outputs and power losses have a positive sign. Mechanical power input by the drive motor is given a negative sign.

7. Comparison of the measured and calculated engine performance

The performance of the developed pulse tube engine was measured for different filling pressures, heater temperatures and operating frequencies. The observations are compared with the corresponding calculated predictions. To allow the identification of

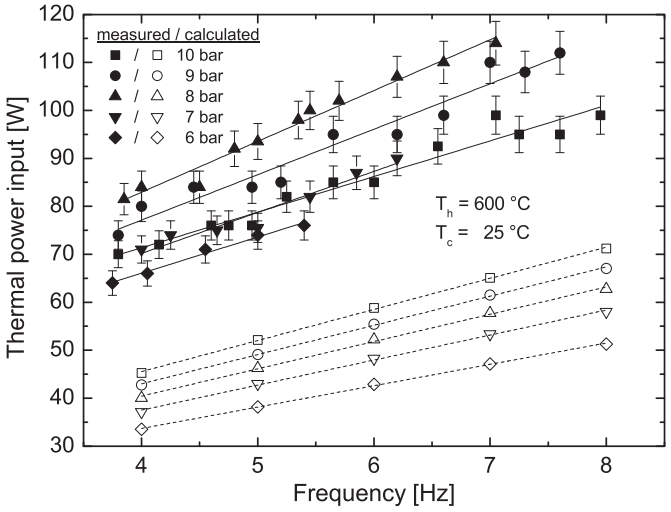

Fig. 7. Calculated and measured thermal power input as functions of the operating frequency for different filling pressures.

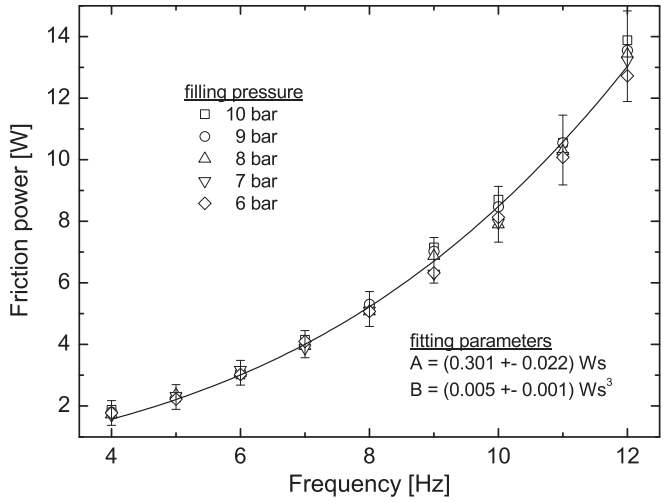

Fig. 8. Measured power consumption due to mechanical friction in the cylinder, bearings and crank mechanism as functions of the operating frequency for different filling pressures. To avoid too many lines in the plot the error bars are only shown for the measured power consumption at 8 bar.

loss mechanisms all measurements were done for opened and closed valve V_1.

7.1. Measured shaft power output and efficiency

The operating conditions of the engine were the same as in Section 6.1. The measured shaft power P_{sh} and efficiency η_{sh} for $T_h = 600$ °C and filling pressures of 6 bar, 8 bar and 10 bar are shown in Fig. 9. The efficiency is calculated with $\eta_{sh} = P_{sh}/\dot{Q}_{in}$, where $\dot{Q}_{in}$ is the measured electrical power consumption of the heater. As shown in Section 6.1 the calculated thermal power input is between 40% and 95% lower than the measured value. Thus, the thermal power delivered to the working gas is smaller leading to a lower efficiency than what was predicted. However, power and efficiency increase with increasing filling pressure. For a given pressure the peak frequency of the power is slightly higher than the peak frequency of the efficiency. Both values increase with increasing filling pressure. Having a filling pressure of 10 bar, the highest shaft power of about 0.9 W and an efficiency of about 1.2% is produced at a frequency of 5 Hz. According to Section 6.2 the friction power loss at a frequency of 5 Hz is 2.2 W.

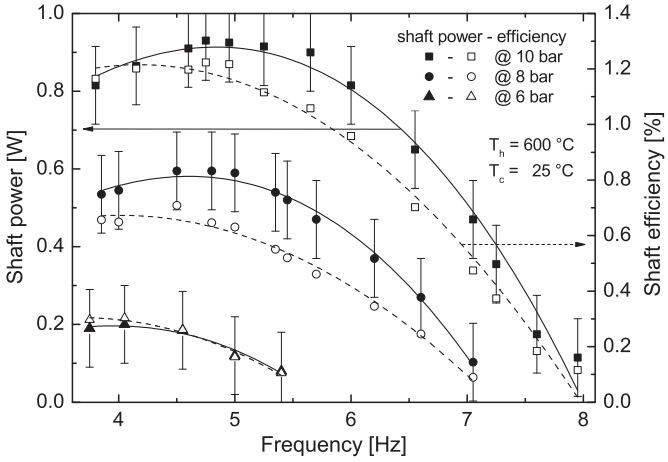

Fig. 9. Measured shaft power output and efficiency as functions of the operating frequency for different filling pressures. To avoid too many lines in the plot the error bars of the measured shaft efficiencies are not shown.

7.2. Measured versus calculated net power output and efficiency

The net power of the engine was obtained experimentally from the difference of the measured power consumption of the motored uncompressed engine (V_1 opened) and the motored compressed engine (V_1 closed). In the uncompressed case, the drive motor has to deliver power P_{sh} to the shaft, which equals the power loss due to mechanical friction $P_{l,ext}$ in the crank shaft and the cylinder. In the compressed case, the amount of power delivered by the drive motor is reduced by the net power output P_n produced by the pulse tube engine. The net power is calculated from $P_n = P_{sh} + P_{l,ext}$ and the net efficiency is calculated with $\eta_n = P_n/\dot{Q}_{in}$, where P_n is the measured net power and $\dot{Q}_{in}$ the heat power input to the gas obtained from the calculation. Measurements and calculations were performed for heat input temperatures of 200 °C, 400 °C and 600 °C, and filling pressures of 6 bar, 8 bar and 10 bar.

A comparison of the measured and calculated results is given in Fig. 10. The filled symbols represent the measured and the unfilled symbols the calculated net power outputs and efficiencies. Within the restricted accuracy of a one-dimensional model, the calculated power outputs match well with the experimental results. At all filling pressures the relative difference in the calculated and measured net power outputs is for $T_h = 400$ °C and $T_h = 600$ °C smaller than 40%. Having a heat input temperature of $T_h = 200$ °C, the relative difference is very high. A maximum error of 465% occurs at $T_h = 200$ °C, $p_f = 6$ bar and $f = 8$ Hz. Due to its low absolute value, the uncertainty of the calculated net efficiency is quite high.

The modeling error was estimated to about 20%. The maximum relative uncertainty of the measured net power is about 11%, and since the electrical drive motor is used for the measurements the minimum absolute error of the measured net power is 0.4 W (compare to Table 2). The total relative difference of the net power outputs of calculation and experiment is thus about 31%. The error for $T_h = 400$ °C and $T_h = 600$ °C has the magnitude of this uncertainty. Since the net power output for $T_h = 200$ °C is smaller than 0.4 W, the obtained relative error can be very high, but is still within the range of the measurement uncertainty. With increasing frequencies, the measured net power increases more strongly than the calculated net power. This could be due to an increase in the heat transfer rate because of flow transition from laminar to turbulent, which is not captured sufficiently by the model.

The engine provides a net power output for all heat input temperatures and filling pressures, which increases with temperature and pressure. The increase slows down strongly for higher temperatures, such that the temperature has no significant influence on the efficiency anymore. This result implies that with increasing temperature difference, more heat energy is dumped due to an enthalpy flow from the hot to the cold side of the pulse tube. For $T_h = 600$ °C, $p_f = 6$ bar and $f = 9$ Hz the engine has a maximum net efficiency of about 8%. The peak of the net power is always at a higher frequency than the peak of the net efficiency. Compared to the shaft power and efficiency, the net power and efficiency have their peak values about 5 Hz higher. This is due to the power dissipation in the cylinder and the crank mechanism (see Section 6.2).

7.3. Internal power loss and gross power output

The functional principle of the pulse tube engine is based on an intrinsically irreversible thermodynamic cycle [13]. Gross power is produced due to an irreversible thermal relaxation in the pulse tube.

Fig. 11 shows the calculated pV-diagram of the pulse tube engine for $p_f = 10$ bar, $f = 8$ Hz, $T_h = 600$ °C and $T_c = 25$ °C. The engine operates between minimum and maximum pressure, p_{min} and p_{max}, respectively. Applying a global polytropic model [14] to the

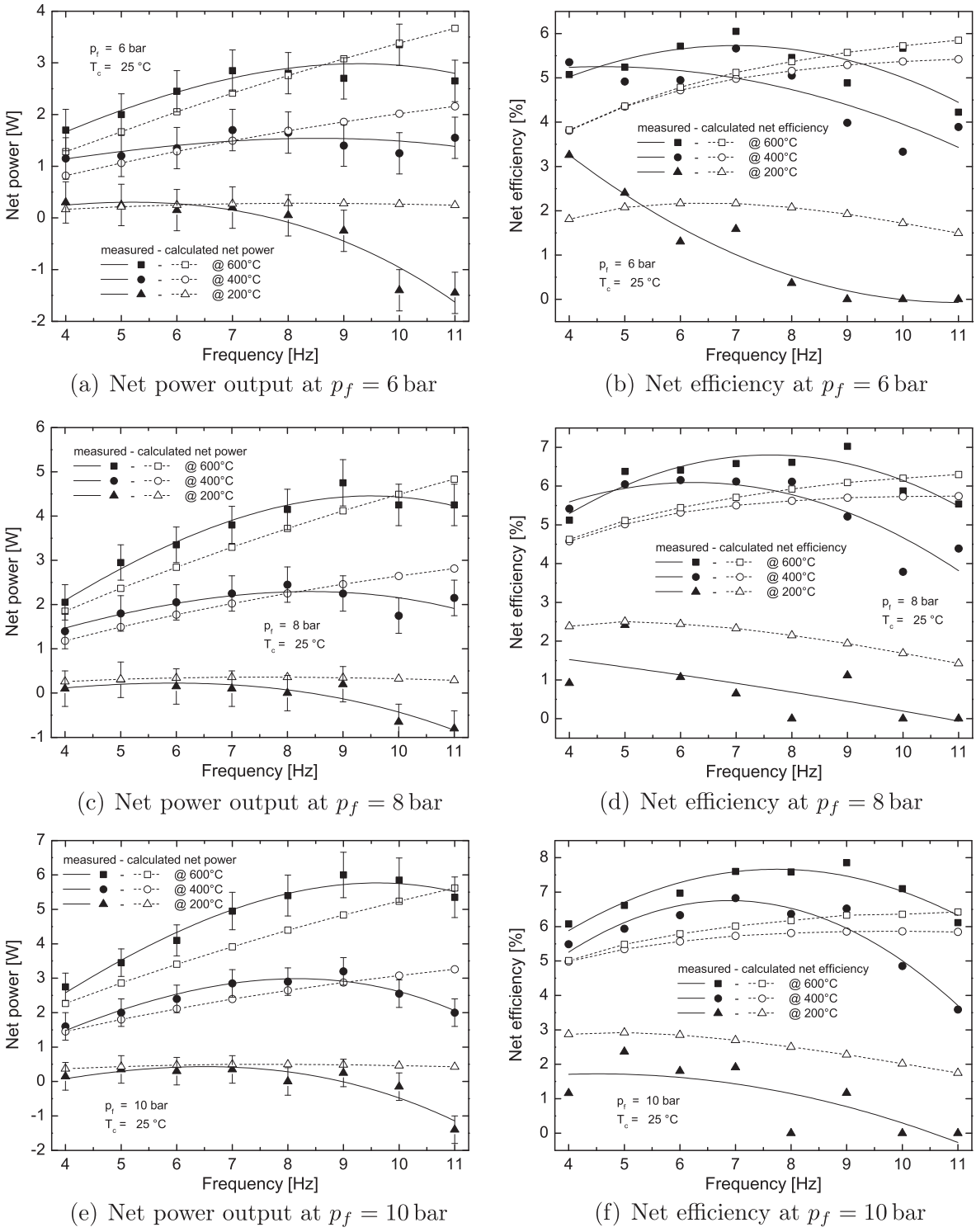

(a) Net power output at $p_f = 6\,\text{bar}$ (b) Net efficiency at $p_f = 6\,\text{bar}$

(c) Net power output at $p_f = 8\,\text{bar}$ (d) Net efficiency at $p_f = 8\,\text{bar}$

(e) Net power output at $p_f = 10\,\text{bar}$ (f) Net efficiency at $p_f = 10\,\text{bar}$

Fig. 10. Calculated and measured net power output and efficiency as functions of the operating frequency for different filling pressures and heat input temperatures. To avoid too many lines in the plots the error bars of the measured net efficiencies are not shown.

entire engine, a polytropic compression with the polytropic exponent $n_p^c(V)$ takes place from BDC to TDC. In the opposite direction a polytropic expansion with the polytropic exponent $n_p^e(V)$ occurs. Since the function $n_p^c(V)$ differs from the function $n_p^e(V)$ the engine is able to provide a gross power output.

With the ratio of the maximum to the minimum engine gas volume $V_{\max}/V_{\min} = 1.26$ and the observed pressure ratio of $\Pi = 1.34$, the mean polytropic exponent n_p can be obtained from

$$\Pi = \left(\frac{V_{\max}}{V_{\min}}\right)^{n_p} \tag{21}$$

to be $n_p = 1.27$. The working gas helium has a mean adiabatic exponent of $\kappa = 1.67$. Thus, the global compression and expansion

processes tend to be close to isothermal behavior ($n_p = 1$). Using this result, the gross power can be estimated with an isothermal model of the compression and expansion processes in combination with thermal (isochoric) relaxation occurring at TDC and BDC. Introducing the temperature ratio $\tau = T_h/T_c$ and the minimal temperature ratio $\tau_0 > 1$, above which the engine is providing a power output, the gross power can be approximated with

$$P_g = a\left(f, p_f, T\right)\left(\frac{\tau - \tau_0}{\tau + 1}\right), \tag{22}$$

where a, in general, is a function of geometry parameters, working gas properties, the operating frequency f, filling pressure p_f and temperature T.

The total internal power loss – also a function of f, p_f, T, geometry parameters and working gas properties – can be written as $P_{l,\mathrm{int}} = b(f,p_f,T)$. The net power output of the engine is given through

$$P_n = P_g - P_{l,\mathrm{int}}. \tag{23}$$

The influence of the temperature on a, and b is due to the temperature dependency of the working gas properties. Assuming a perfect gas, the net power becomes

$$P_n = \overline{a\left(f, p_f\right)}\left(\frac{\tau - \tau_0}{\tau + 1}\right) - \overline{b\left(f, p_f\right)}. \tag{24}$$

For a fixed frequency and filling pressure, the coefficients $\overline{a}$, $\overline{b}$ and the minimal temperature ratio τ_0 can be obtained from the experiment. To do so, the net power output was measured for filling pressures of 6 bar, 8 bar and 10 bar, and frequencies from 4 Hz to 12 Hz. For each pair of (f, p_f) the engine was motored at heat input temperatures between 40 °C and 600 °C. The measured net power P_n is plotted versus the temperature ratio τ. For $f = 8$ Hz the results are shown in Fig. 12. For all investigated filling pressures the net power becomes zero at $\tau = 1.62 \pm 0.1$. Since the internal power loss is a function of the filling pressure, and for all investigated pressures the net power equals zero at $\tau = 1.62$, the internal power loss has to be zero at $\tau = 1.62$, and thus $P_n(\tau = 1.62) = P_g(\tau = \tau_0) = 0$, resulting in $\tau_0 = 1.62 \pm 0.1$. Hence, the engine needs a minimal temperature difference of $T_h - T_c \approx 185$ K to provide a power output. The net power as a function of τ is adapted with Eq. (24), where for the minimal temperature ratio the value $\tau_0 = 1.62$ is used.

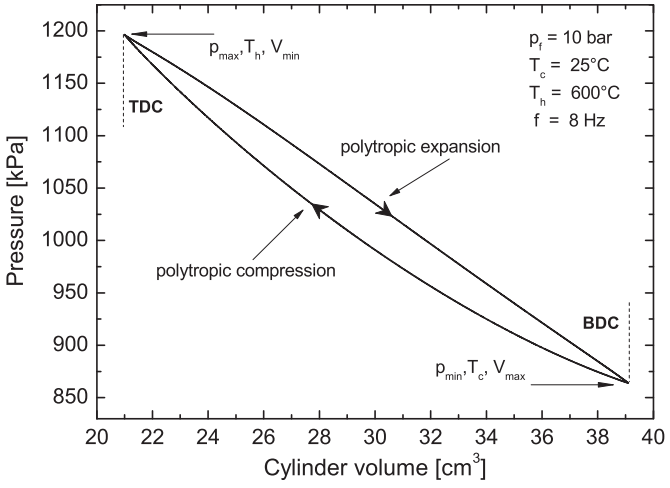

Fig. 11. Calculated pV-diagram at a filling pressure of 10 bar and a operating frequency of 8 Hz.

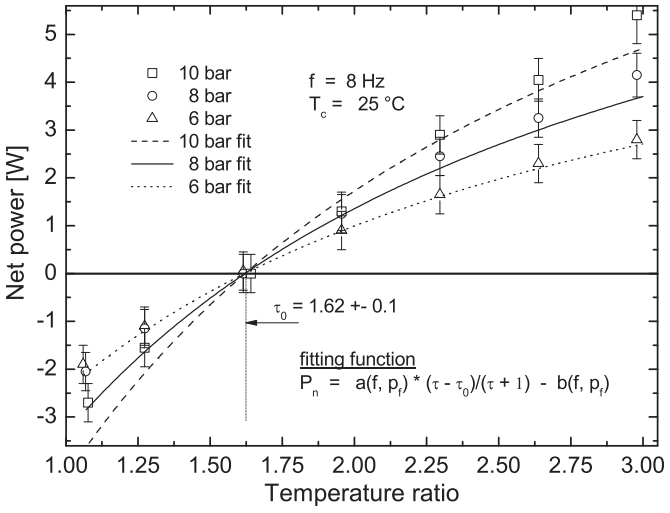

Fig. 12. Fit of the measured net power output as a function of the temperature ratio for different filling pressures and a operating frequency of 8 Hz.

With the fitted coefficients $\overline{a}$ and $\overline{b}$, the total internal power loss $P_{l,\mathrm{int}}$ and the gross power P_g can be calculated.

For filling pressures of 6 bar, 8 bar and 10 bar, and operating frequencies higher than 8 Hz, the internal power loss depending on the operating frequency is shown in Fig. 13. At each frequency, the values of the internal power loss are averaged and adapted with a function $P_{l,\mathrm{int}} \propto f^5$. For operating frequencies lower than 8 Hz the internal power loss is almost zero. Exceeding this frequency, it increases non-linearly with the frequency, but is still quite low.

For $T_h = 600$ °C, and filling pressures between 6 bar and 10 bar, the gross power dependency on the operating frequency is shown in Fig. 14. At all pressures it is increasing linearly with the operating frequency. The gross power also depends linearly on the filling pressure. Thus, the coefficient $\overline{a}$ is directly proportional to the product of f and p_f. This result is obvious since the gross power is proportional to the oscillating mass in the engine. The mass flux itself is directly proportional to the frequency and the filling pressure.

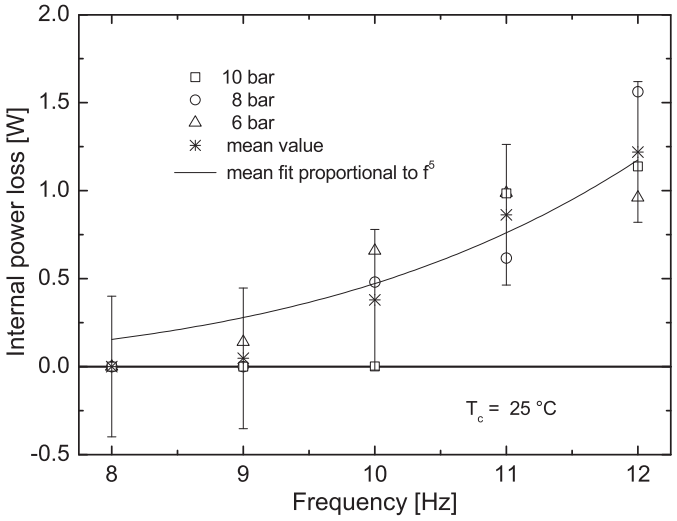

Fig. 13. Measured internal power loss as a function of the operating frequency for different filling pressures. To avoid too many lines in the plot the error bars are only shown for the averaged internal power loss.

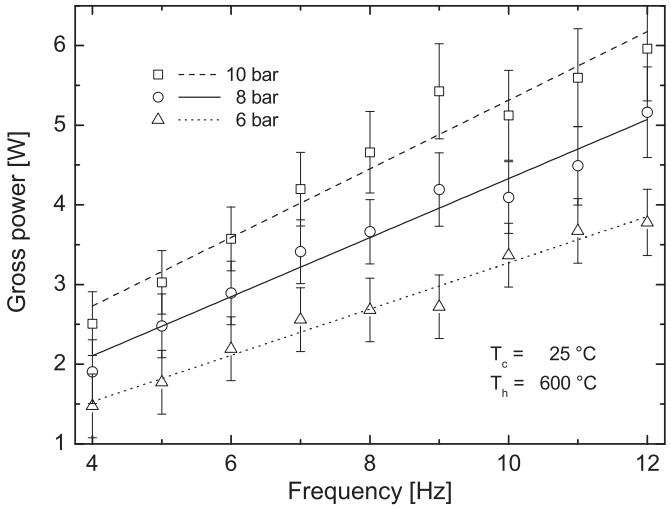

Fig. 14. Measured gross power output as a function of the operating frequency at a heat input temperature of 600 °C and different filling pressures.

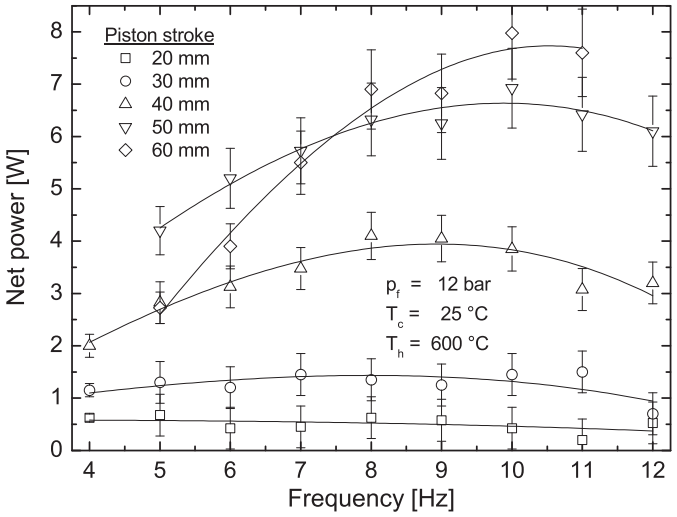

Fig. 16. Measured net power output as a function of the operating frequency for different engine strokes.

Fig. 15 shows the gross power output for a filling pressure of 10 bar and heat input temperatures between 40 °C and 600 °C. In all cases, the observed gross power output increases ($T_h > 200$ °C), respectively decreases ($T_h < 200$ °C), linearly with the operating frequency. The engine is not operating for heat input temperatures lower than 200 °C.

8. Influence of design parameters on the engine performance

In Ref. [8] it was shown that the engine performance strongly depends on the compression ratio and distribution ratio (see Section 4.2 for their definitions). In this work these theoretical predictions are investigated experimentally and compared to the results of the simulation model. Additionally the influence of the cold heat exchanger area is studied experimentally. The model calibration (see Section 5) is kept at the values of the previously investigated engine geometry. Thus, the calculation results are quantitatively not comparable to the experimental observations. Nevertheless, the tendency of the performance by changing the engine geometry can be reproduced by the model as well.

8.1. Compression ratio

The engine was motored for strokes between 20 mm and 60 mm. Fig. 16 shows the resulting measured net power outputs for operating frequencies between 4 Hz and 12 Hz. The highest values are observed for a stroke of 60 mm. With the experimental set-up, power outputs at higher strokes than this value were impossible to measure reliably.

A comparison of the measured and calculated net power outputs depending on the compression ratio according to Eq. (17) is given in Fig. 17. The operating frequency of the engine is 8 Hz, which is slightly lower than the net power's peak frequency. Observation and calculation show an increasing net power for higher compression ratios. Thus, on a qualitative basis, the model reproduces well the observed engine behavior. For $T_h = 400$ °C the mismatch between calculation and observation is higher due to lower power outputs and thus a stronger influence of the modeling error. The experiment shows an optimal compression ratio of 0.47 (50 mm stroke) for $T_h = 400$ °C and 0.56 (60 mm stroke) for

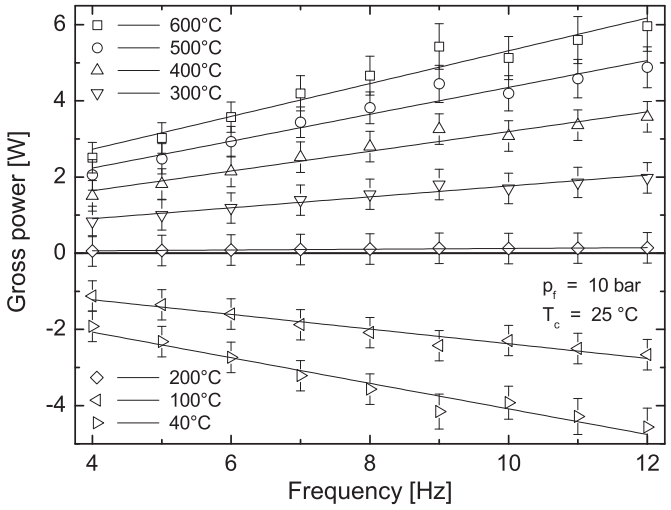

Fig. 15. Measured gross power output as a function of the operating frequency at a filling pressure of 10 bar and different heat input temperatures.

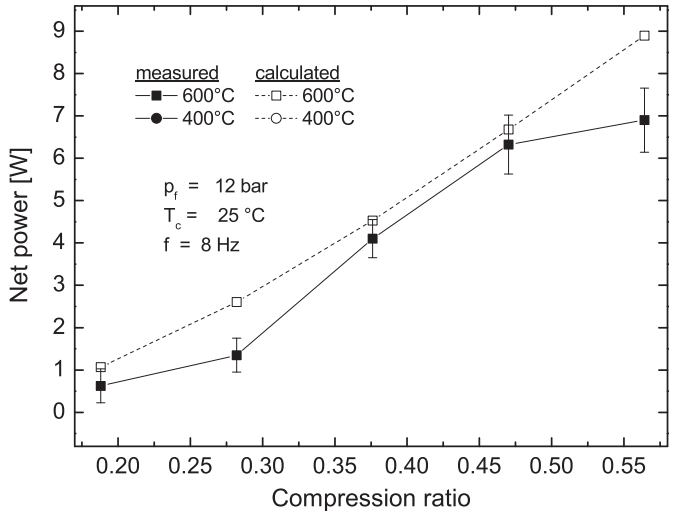

Fig. 17. Calculated and measured net power output as functions of the compression ratio for different heat input temperatures.

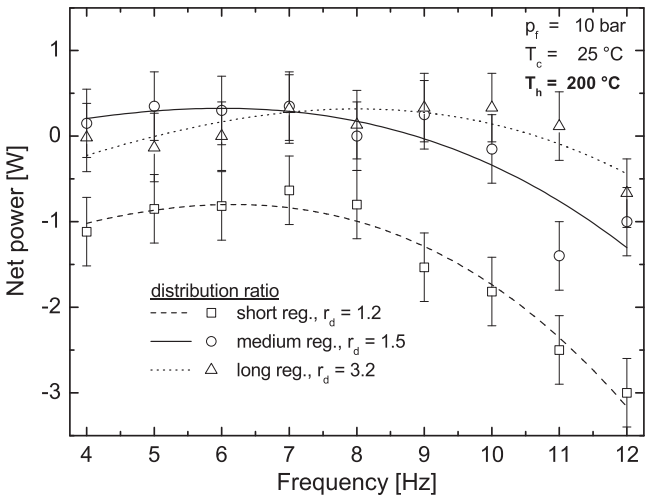

(a) $T_h = 200\,^{\circ}\mathrm{C}$

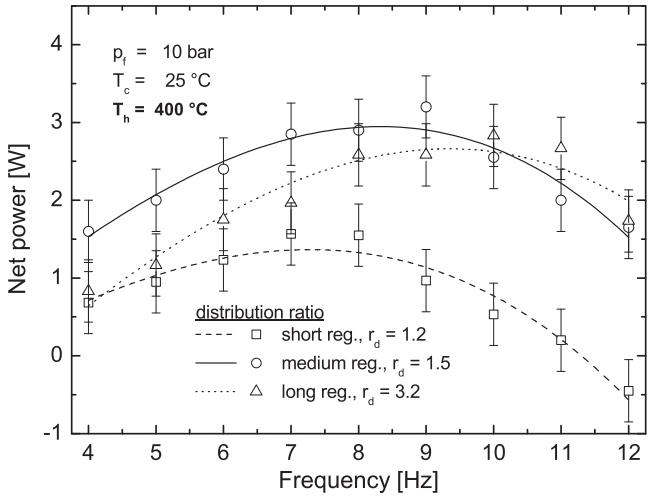

(b) $T_h = 400\,^{\circ}\mathrm{C}$

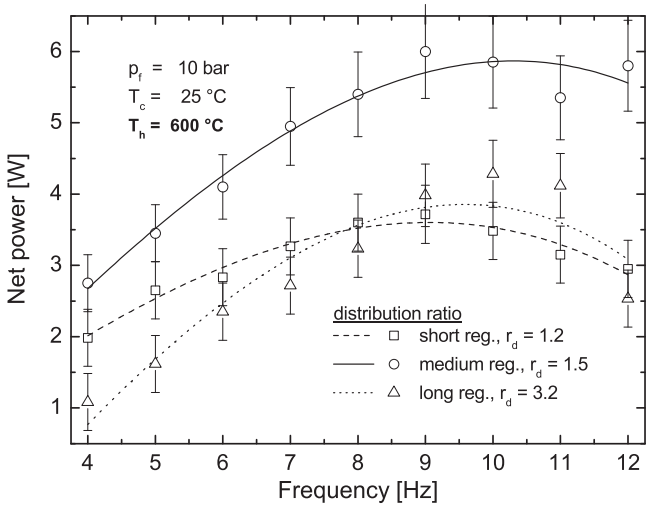

(c) $T_h = 600\,^{\circ}\mathrm{C}$

Fig. 18. Measured net power output as a function of the operating frequency for different distribution ratios and heat input temperatures.

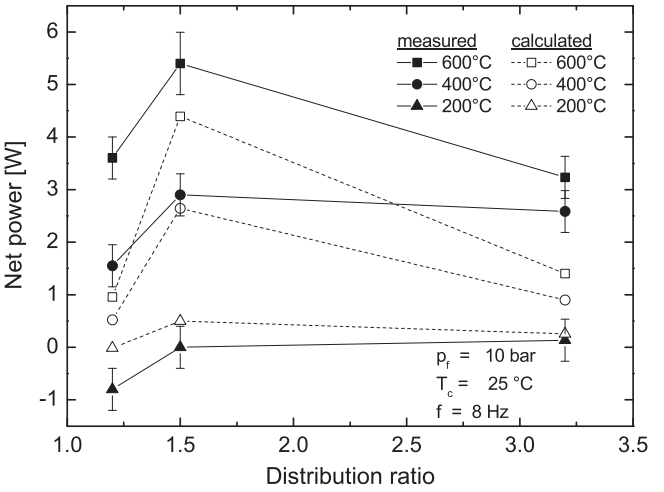

Fig. 19. Calculated and measured net power output as functions of the distribution ratio for different heat input temperatures.

$T_h = 600\,^{\circ}\mathrm{C}$. This observation is in accordance with the theoretical predictions in Ref. [8], Fig. 9. The compression ratio introduced in Ref. [8] is the compression ratio defined in Eq. (17) plus one. However, higher heat input temperatures allow higher compression ratios and a higher power output.

8.2. Distribution ratio

To study the influence of the distribution ratio three regenerators with lengths of 111 mm, 122 mm and 143 mm are manufactured and placed into the 230 mm long stainless steel tube. The resulting lengths of the pulse tube are 76 mm, 68 mm and 44 mm. The flanges of the 122 mm regenerator version are in total 3 mm longer than in the two other regenerator versions. With these dimensions of pulse tube and regenerator the distribution ratios according to Eq. (18) are $r_d = 1.2$ (short regenerator), $r_d = 1.5$ (medium regenerator) and $r_d = 3.2$ (long regenerator). For the motored engine, the measured net power outputs at heat input temperatures of 200 °C, 400 °C and 600 °C

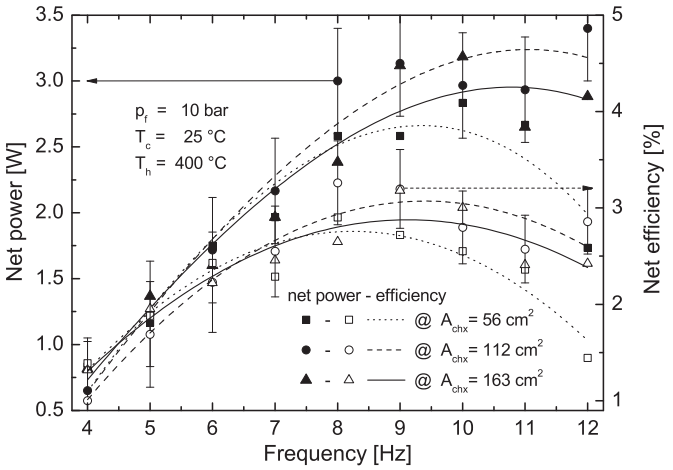

Fig. 20. Measured net power output and efficiency as functions of the operating frequency for different cold heat exchanger areas. To avoid too many lines in the plot the error bars are only shown for the measured values at $A_{chx} = 112\ \mathrm{cm}^2$.

are shown in Fig. 18. For all temperatures the short regenerator always leads to the lowest power outputs. At $T_h = 400$ °C the medium and the long regenerator lead to comparable power outputs. For lower temperatures the long regenerator becomes advantageous and for higher temperatures the medium regenerator. An ideal engine having a high value of r_d (long regenerator) has a high thermodynamic asymmetry and is according to [8], Fig. 10 functioning best. In the real engine the long regenerator is accompanied by a short pulse tube. Thus, the hot heat exchanger is closer to the cold heat exchanger. A higher portion of the applied thermal power flows directly to cold heat exchanger and is released unused. This power loss increases for higher heat input temperatures and leads to the observed better engine performance with a medium regenerator length.

In Fig. 19 the calculated and measured net power outputs depending on the distribution ratio for an operating frequency of 8 Hz are compared. For all temperatures the calculations predict an even stronger dependency of the net power on the distribution ratio than the experiment shows. The best match is given for the medium size regenerator. The model was calibrated for this case. Nevertheless, the existence of an optimal distribution ratio is evident from measurement and calculation.

8.3. Area of the cold heat exchanger

It was claimed that the cold heat exchanger chx_1 needs a certain heat transfer rate for optimal engine operation. To check this its heat transfer area A_{chx} was modified experimentally. Three cold heat exchangers were manufactured with heat transfer areas of 56 cm^2, 112 cm^2 and 163 cm^2, respectively. For $T_h = 400$ °C the measured net power output as well as the net efficiency are shown in Fig. 20.

At frequencies lower than 8 Hz the influence of the cold heat exchanger area on the engine performance is small. Having higher operating frequencies the heat exchanger with an area of 112 cm^2 delivers best performance results. The observation shows the importance of a careful design of the cold heat exchanger. In contrast to Stirling engines a maximized heat transfer capability does not lead to the best pulse tube engine performance.

9. Conclusions

The present study clarifies the working principle of the pulse tube engine and shows its potential and limitations. The developed numerical and experimental tools could be used successfully to built up a pressurized working engine and characterize its mode of operation under different heat input temperatures, filling pressures and operating frequencies. Model and experiment deliver comparable engine performances.

The shaft power, the net power and the gross power of the engine could be obtained from measurement and calculation. Power losses were quantified. The investigated engine provides a maximum net power output of about 6 W at a frequency of 9 Hz and a net efficiency of about 8%.

Theoretical predictions of a prior study concerning the influence of design parameters could be proven experimentally. The found optimal design parameters will help to develop future pulse tube engines.

This work forms a basis for further studies of that kind of heat engine. The measured and calculated engine behavior for different heat input temperatures shows that the pulse tube engine has a potential application at low temperature heat sources (about 300 °C). At this temperature level its practical performance will be comparable to other prime movers, such as Stirling engines. The theoretical disadvantage of the pulse tube engine process based on an intrinsically irreversible thermodynamic cycle could be compensated by its practical advantages, such as a comparably low flow friction power loss and the simple mechanical gear system associated with its low production costs.

Acknowledgments

The presented work was supported by the German Federal Environmental Foundation. All simulations were done using SimulationX, kindly sponsored by ITI GmbH Dresden, Germany.

References

[1] Gifford WE, Longsworth RC. Pulse tube refrigeration process. In Advances in cryogenic engineering, vol. 10. New York: Plenum Press; 196569.
[2] Chen NCJ, West CD. A single-cylinder valveless heat engine. In: Proceedings of the 22nd intersociety energy conversion engineering conference 1987. p. 1386–9.
[3] Tailer PL. Thermal lag machine. Patent US 5,414,997; 1995.
[4] Organ AJ. The air engine: Stirling cycle power for a sustainable future. Cambridge: Woodhead Publishing; 2007107–31.
[5] Hamaguchi K, Ushijima Y, Hiratsuka Y. Basic characteristics of pulse tube engine. In: Proceedings of the 12th ISEC 2005. p. 275–84.
[6] Hamaguchi K, Futagi H, Yazaki T, Hiratsuka Y. Measurement of work generation and improvement in performance of a pulse tube engine. Journal of Power and Energy Systems 2008;2(5):1267–75.
[7] Yoshida T, Yazaki T, Futaki H, Hamaguchi K, Biwa T. Work flux density measurements in a pulse tube engine. Applied Physics Letters 2009;95.
[8] Moldenhauer S, Thess A, Holtmann C, Fernándes-Aballí C. Thermodynamic analysis of a pulse tube engine. Journal of Energy Conversion and Management 2013;65:810–8.
[9] VDI–Wärmeatlas, vol. 7. Düsseldorf: VDI–Verlag GmbH; 1994, Gb 1–8.
[10] Kays WM, London AL. Hochleistungswärmeübertrager. Berlin: Akademie-Verlag; 1973.
[11] Ward JC. Turbulent flow in porous media. ASCE Journal of the Hydraulics Division 1964;90:1–12.
[12] Macdonald IF, El-Sayed MS, Mow K, Dullien FAL. Flow through porous media–Ergun equation revisited. Industrial and Engineering Chemistry Fundamentals 1979;18(3):199–208.
[13] Wheatley J, Hofler T, Swift GW, Migliori A. Experiments with an intrinsically irreversible acoustic heat engine. Physical Review Letters 1983;50(7): 499–502.
[14] Gyftopoulos EP, Beretta GP. Thermodynamics, foundations and applications. New York: Dover Publications; 2005.